

Non-gravitational acceleration in the trajectory of 1I/2017 U1 (‘Oumuamua)

Marco Micheli^{1,2*}, Davide Farnocchia³, Karen J. Meech⁴, Marc W. Buie⁵, Olivier R. Hainaut⁶, Dina Prialnik⁷, Norbert Schörghofer⁸, Harold A. Weaver⁹, Paul W. Chodas³, Jan T. Kleyna⁴, Robert Weryk⁴, Richard J. Wainscoat⁴, Harald Ebeling⁴, Jacqueline V. Keane⁴, Kenneth C. Chambers⁴, Detlef Koschny^{1,10,11} & Anastassios E. Petropoulos³

‘Oumuamua (1I/2017 U1) is the first known object of interstellar origin to have entered the Solar System on an unbound and hyperbolic trajectory with respect to the Sun¹. Various physical observations collected during its visit to the Solar System showed that it has an unusually elongated shape and a tumbling rotation state^{1–4} and that the physical properties of its surface resemble those of cometary nuclei^{5,6}, even though it showed no evidence of cometary activity^{1,5,7}. The motion of all celestial bodies is governed mostly by gravity, but the trajectories of comets can also be affected by non-gravitational forces due to cometary outgassing⁸. Because non-gravitational accelerations are at least three to four orders of magnitude weaker than gravitational acceleration, the detection of any deviation from a purely gravity-driven trajectory requires high-quality astrometry over a long arc. As a result, non-gravitational effects have been measured on only a limited subset of the small-body population⁹. Here we report the detection, at 30σ significance, of non-gravitational acceleration in the motion of ‘Oumuamua. We analyse imaging data from extensive observations by ground-based and orbiting facilities. This analysis rules out systematic biases and shows that all astrometric data can be described once a non-gravitational component representing a heliocentric radial acceleration proportional to r^{-2} or r^{-1} (where r is the heliocentric distance) is included in the model. After ruling out solar-radiation pressure, drag- and friction-like forces, interaction with solar wind for a highly magnetized object, and geometric effects originating from ‘Oumuamua potentially being composed of several spatially separated bodies or having a pronounced offset between its photocentre and centre of mass, we find comet-like outgassing to be a physically viable explanation, provided that ‘Oumuamua has thermal properties similar to comets.

The object now known as 1I/‘Oumuamua was discovered on 2017 October 19 by the Pan-STARRS1 survey^{10,11}. Within a few days, additional observations collected with the European Space Agency (ESA) Optical Ground Station (OGS) telescope and at other observatories, together with pre-discovery data from Pan-STARRS1, allowed the determination of a preliminary orbit that was highly hyperbolic (eccentricity of 1.2). Such an orbit identified the object as originating from outside the Solar System¹ and approaching from the direction of the constellation Lyra, with an asymptotic inbound velocity of around 26 km s^{-1} .

This extreme eccentricity also led the Minor Planet Center to classify the object as a comet initially¹². However, this classification was later withdrawn when images obtained immediately after discovery using the Canada–France–Hawaii Telescope (CFHT) and, in the subsequent days, the European Southern Observatory (ESO) Very Large Telescope (VLT) and the Gemini South (GS) Telescope, both 8-metre-class facilities, found no sign of coma despite optimal seeing conditions (see Fig. 1 and

discussion in Methods). In addition, spectroscopic data obtained^{5,7} at around the same time showed no evidence of identifiable gas emission in the visible-wavelength region of the spectrum. Although the object has a surface reflectivity similar to comets^{1,5,7}, all other observational evidence available at the time suggested that ‘Oumuamua was probably inactive and of asteroidal nature, despite predictions that cometary interstellar objects should be the easier to discover because they brighten more than asteroids^{1,13}.

In parallel with physical and compositional studies, our team continued to image ‘Oumuamua to constrain its trajectory further through astrometric measurements. As ‘Oumuamua faded, we obtained data with CFHT, VLT and the Hubble Space Telescope (HST; see Methods). A final set of images was obtained with HST in early 2018 for the purpose of extracting high-precision astrometry. The resulting dataset provides dense coverage from discovery to 2018 January 2, when the object became fainter than $V \approx 27$ at a heliocentric distance of 2.9 AU.

We analysed the full observational dataset, which includes 177 ground-based and 30 HST-based astrometric positions (for a total of 414 scalar measurements), applying the procedures and assumptions discussed in Methods. Our analysis shows that the observed orbital arc cannot be fitted in its entirety by a trajectory governed solely by gravitational forces due to the Sun, the eight planets, the Moon, Pluto, the 16 largest bodies in the asteroid main belt and relativistic effects¹⁴. As shown in Fig. 2a, the residuals in right ascension and declination of the best-fitting gravity-only trajectory are incompatible with the formal uncertainties: ten data points deviate by more than 5σ in at least one coordinate, and 25 are discrepant by more than 3σ . Furthermore, the offsets (as large as $22''$ for the 2017 October 14 Catalina observation) are not distributed randomly but show clear trends along the trajectory.

To improve the description of the trajectory of ‘Oumuamua, we included a radial acceleration term $A_1 g(r)$ in the model⁸, where A_1 is a free fit parameter, r is the heliocentric distance and $g(r)$ is set to be proportional to r^{-2} , matching the decrease of solar flux with distance, with $g(1 \text{ AU}) = 1$. As shown in Fig. 2b, the addition of this term allows us to explain the data for $A_1 = (4.92 \pm 0.16) \times 10^{-6} \text{ m s}^{-2}$, which corresponds to a formal detection of non-gravitational acceleration with a significance of about 30σ . Additional analyses, discussed in greater detail in Methods, further support our finding that the non-gravitational acceleration is preferentially directed radially away from the Sun, and allow both the aforementioned r^{-2} dependency and a less steep r^{-1} law. By contrast, a constant acceleration independent of distance is strongly disfavoured, regardless of direction (radial, along the instantaneous velocity vector of ‘Oumuamua or inertially fixed). Table 1 reports the χ^2 and reduced χ^2 (χ_r^2) statistics for the astrometric fits of each of the models tested (see Methods for details). We used

¹ESA SSA-NEO Coordination Centre, Frascati, Italy. ²INAF—Osservatorio Astronomico di Roma, Monte Porzio Catone, Italy. ³Jet Propulsion Laboratory, California Institute of Technology, Pasadena, CA, USA. ⁴Institute for Astronomy, University of Hawai‘i, Honolulu, HI, USA. ⁵Southwest Research Institute, Boulder, CO, USA. ⁶European Southern Observatory, Garching bei München, Germany. ⁷School of Geosciences, Sackler Faculty of Exact Sciences, Tel Aviv University, Ramat Aviv, Israel. ⁸Planetary Science Institute, Tucson, AZ, USA. ⁹The Johns Hopkins University Applied Physics Laboratory, Space Exploration Sector, Laurel, MD, USA. ¹⁰ESTEC, European Space Agency, Noordwijk, The Netherlands. ¹¹Chair of Astronautics, Technical University of Munich, Garching bei München, Germany. *e-mail: marco.micheli@esa.int

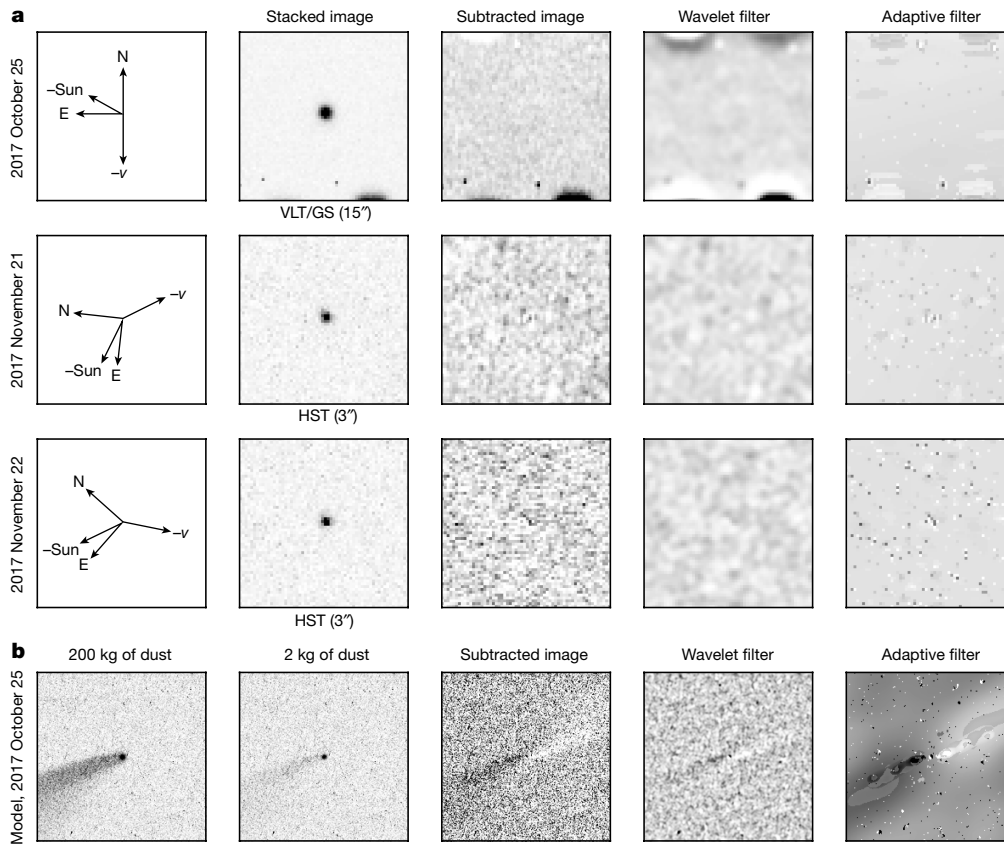


Fig. 1 | Deep stacked images for dust detection. **a**, For each date we show the image orientation (–Sun, anti-solar direction; – v , anti-motion direction), the stacked image (telescope and size of the image are listed below the image), a self-subtracted image (see Methods), and the image after application of a wavelet or adaptive filter to enhance low-surface-brightness features. No dust is visible. **b**, Images from a model

with an artificial cometary feature that matches the October geometry demonstrate the sensitivity of the image enhancement: a very strong dust feature is evident when 200 kg of dust is used in the point spread function (PSF) region (left-most panel); the other panels show the same feature scaled to 2 kg of dust in the PSF region (twice the observed ‘Oumuamua limit) and the image processed in the same manner as the real data.

conservative estimates for the measurement uncertainties that serve as data weights to mitigate the effect of systematic errors, for example, due to star catalogue biases, field-of-view distortions, clock errors or the absence of uncertainty information (for astrometry produced by others). As a result, the χ^2 and χ^2_{ν} values listed are lower than would be expected for purely Gaussian noise, and the correspondingly larger error bars that we derive more safely capture the actual uncertainties in the estimated parameters.

We performed a series of tests, also discussed in greater detail in Methods, which confirm that the non-gravitational signature is neither an artefact caused by some subset of the observations nor the result of overall systematic biases unaccounted for in the analysis. Even a substantial inflation of the assumed error bars in the astrometry, applied to reflect possible catalogue biases or uncorrected distortions, still results in a significant detection. In addition, the non-gravitational acceleration is clearly detected both in ground-based observations alone and

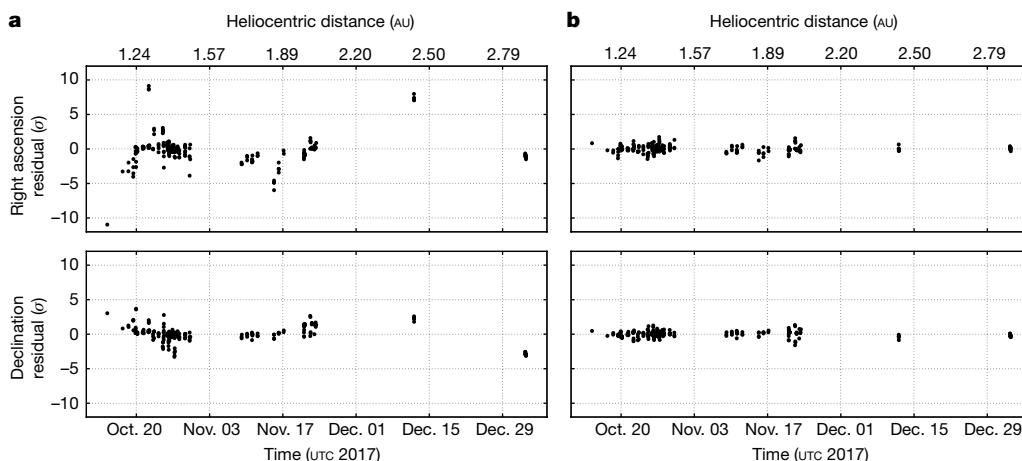


Fig. 2 | Astrometric residuals of ‘Oumuamua observations. **a**, **b**, Normalized residuals for right ascension and declination compared to a gravity-only solution (**a**) and a solution that includes a non-gravitational radial

acceleration of $A_1 r^{-2}$ (**b**). Because each residual is normalized to its formal uncertainty, each data point has a 1σ error bar (not shown) equal to 1 on this scale.

Table 1 | Fits for different non-gravitational models

Model	Number of parameters	χ^2	χ^2_ν
Gravity-only	6	1.031×10^3	2.53
(1) Impulsive change in velocity	10	117	0.29
(2) Pure radial acceleration, $A_1 g(r) \propto r^{-k}$, $k \in \{0, 1, 2, 3\}$	7	99, 80, 81, 98	0.24, 0.20, 0.20, 0.24
(3) RTN decomposition, $[A_1, A_2, A_3]g(r) \propto r^{-k}$, $k \in \{0, 1, 2, 3\}$	9	90, 80, 78, 87	0.22, 0.20, 0.19, 0.21
(4) ACN decomposition, $[A_A, A_C, A_N]g(r) \propto r^{-k}$, $k \in \{0, 1, 2, 3\}$	9	104, 85, 77, 83	0.26, 0.21, 0.19, 0.21
(5) Pure along-track acceleration, $A_A g(r) \propto r^{-k}$, $k \in \{0, 1, 2, 3\}$	7	1.031×10^3 , 1.025×10^3 , 1.002×10^3 , 963	2.53, 2.52, 2.46, 2.37
(6) Constant, inertially fixed acceleration vector	9	116	0.29
(7a) Pure radial acceleration, $A_1 g_{CO}(r)$	7	84	0.21
(7b) Pure radial acceleration, $A_1 g_{H_2O}(r)$	7	111	0.27
(7c) RTN decomposition, $[A_1, A_2, A_3]g_{CO}(r)$	9	79	0.19
(7d) RTN decomposition, $[A_1, A_2, A_3]g_{H_2O}(r)$	9	89	0.22
(7e) RTN decomposition, $[A_1, A_2, A_3]g_{H_2O}(r), \Delta T$	10	86	0.21

For reference, we list the values for a gravity-only model of the trajectory in addition to those for the different non-gravitational models. In addition to a model involving an impulsive change in velocity, we consider continuous non-gravitational accelerations $g(r)$ with a dependence on the heliocentric distance r that is either a power law or, for H₂O or CO volatiles (g_{H_2O} or g_{CO}), based on cometary outgassing models^{29,30}. The acceleration vector can be inertially fixed or decomposed in either the radial, transverse, normal (RTN; components indicated as $A_1 g(r)$, $A_2 g(r)$ and $A_3 g(r)$, respectively) or the along-track, cross-track, normal (ACN; components indicated as $A_A g(r)$, $A_C g(r)$ and $A_N g(r)$, respectively) frame. We also test the possibility of a time delay ΔT with respect to perihelion for the peak of the outgassing activity. The numbering of the models refers to the discussion in Methods.

in an HST-only arc complemented with just a few early ground-based high-quality data points.

Exploring various possible explanations for the non-gravitational acceleration that was detected, we find outgassing to be the most physically plausible explanation, although with some caveats. A thermal outgassing model¹⁵, which treats 'Oumuamua like a common cometary nucleus, suggests a non-gravitational force proportional to r^{-2} in the range of distances covered by our observations.

The model predictions for the magnitude and temporal evolution of the non-gravitational acceleration are within a factor of about 2–3 of the observations (see Methods) for a water production rate of $Q_{H_2O} = 4.9 \times 10^{25}$ molecules s^{-1} (or 1.5 kg s^{-1}) near 1.4 AU and an additional contribution from $Q_{CO} = 4.5 \times 10^{25}$ molecules s^{-1} (or 2.1 kg s^{-1}). Outgassing at this level does not conflict with the absence of spectroscopic detections for outgassing of OH, because the values quoted are well below the spectroscopic limits on production rates¹⁶. However, the inferred upper limits for water production at 1.4 AU, which are based on the non-detection of CN⁷ and assumed Solar System abundances for Q_{CN}/Q_{OH} ¹⁷, show that 'Oumuamua would need to be substantially depleted in CN (by a factor of more than about 15) relative to water. The model also predicts 0.4 kg s^{-1} of dust production, which should have been detectable in the images. However, if the grains are predominantly larger than a few hundred micrometres to millimetres, they would not have been detected at optical wavelengths (see Methods). In the Solar System, comet 2P/Encke is noteworthy for its lack of small dust near perihelion¹⁸. Cometary behaviour implies that 'Oumuamua must have some internal strength, at least comparable to Solar System comets¹⁹, because asteroid-like densities are ruled out (see Methods).

Alternative explanations for the observed acceleration include (1) solar-radiation pressure, (2) the Yarkovsky effect, (3) friction-like effects aligned with the velocity vector, (4) an impulsive change in velocity, (5) a binary or fragmented object, (6) a photocentre offset or (7) a magnetized object. However, as outlined in the following, these explanation are all either physically unrealistic or insufficient to explain the observed behaviour.

(1) The simplest physical phenomenon that could cause a radial acceleration that follows an r^{-2} dependence and that is directed away

from the Sun is pressure from solar radiation. Such a pressure has been detected for a few small asteroids^{20–23}; however, for 'Oumuamua the magnitude of the observed acceleration implies an unreasonably low bulk density, roughly three to four orders of magnitude below the typical density of Solar System asteroids of comparable size. Additional considerations regarding the plausibility of solar-radiation pressure as an explanation for the non-gravitational motion are presented in Methods.

(2) A rotating body in space experiences a small force due to the anisotropic emission of thermal photons, the so-called Yarkovsky effect²⁴. The resulting perturbation can be excluded as an explanation for the observed acceleration because of its low intensity (at most comparable to that of solar-radiation pressure) and because it mainly affects the motion in the along-track direction, in conflict with our data.

(3) Some dynamical effects, such as friction- or drag-like phenomena, tend to be aligned with the direction of motion and not with the heliocentric radial vector. However, decomposition of the non-gravitational acceleration shows that the respective best-fitting component along the direction of motion is not only insufficient to explain the observations (see Table 1) but also positive, whereas drag-like phenomena would require it to be negative.

(4) Models of the trajectory that include a single impulsive change in velocity, for example, due to a collision, provide a poorer fit to the data (Table 1) than purely radial acceleration. More importantly, we detect the non-gravitational signal even in disjoint subsets of the observed arc, separated at the time of the possible impulse, which makes continuous acceleration a far more likely explanation.

(5) In the case of a binary or fragmented object, the centre of mass of the combined system does in fact follow a purely gravitational trajectory, and the detected non-gravitational signature could be an artefact caused by us tracking only the main component of 'Oumuamua. However, no secondary body or fragment is visible in our data down to a few magnitudes fainter than 'Oumuamua, and any object smaller than the corresponding size limit (roughly 100 times smaller than 'Oumuamua) would be insufficient to explain the observed astrometric offsets.

(6) 'Oumuamua may have surface characteristics that significantly displace the optical photocentre (the position that is measured astrometrically) from the centre of mass. However, even assuming the longest possible extent of 800 m for a low-albedo ($p = 0.04$) object¹, the maximum separation between the two reference points would be approximately 0.005'' at closest approach, several orders of magnitude less than the offset observed for a gravity-only solution.

(7) If 'Oumuamua had a strong magnetic field, then interaction with solar wind could affect its motion^{25,26}. Assuming a dipole field, a plasma-fluid model and typical solar wind speed and proton number density²⁷, we find the resulting acceleration for an object of the nominal size of 'Oumuamua¹ to be only 2×10^{-11} m s^{-2} , too small by a factor of about 10^5 , even if we adopt the high magnetization and density of asteroid (9969) Braille²⁸.

Although this list of possible alternative explanations is not exhaustive, we believe that it covers most of the physical mechanisms worth exploring on the basis of the available data. The models tested here attempt only to describe the dynamical behaviour of 'Oumuamua within the temporal arc covered by the observations. The presence of non-gravitational acceleration and the complexity of the physical explanation proposed by us suggest that any extrapolation to the past and future trajectories of 'Oumuamua outside the modelled arc may be subject to substantial uncertainties.

Outgassing provides the most plausible physical model of the non-gravitational acceleration by postulating that 'Oumuamua behaves like a miniature comet. This hypothesis is consistent with independent results^{5,6} that demonstrate that the spectra and the lack of activity observed are consistent with a cometary body with a thin insulating mantle, and also with the non-gravitational accelerations observed for other Solar System comets (see Extended Data Fig. 1). By establishing the object as an icy body (albeit one with possibly unusual chemical

composition and dust properties), this scenario agrees with the predictions that suggest that only a small fraction of interstellar objects should be asteroidal²⁹. The lack of observed dust lifted from the object by the hypothesized cometary activity can be explained by an atypical dust-grain size distribution that is devoid of small grains, a low dust-to-ice ratio or surface evolution from its long journey. However, these important aspects of the physical nature of 'Oumuamua cannot be resolved conclusively with the existing observations. In situ observations would be essential to reveal unambiguously the nature, origin and physical properties of 'Oumuamua and other interstellar objects that may be discovered in the future. This work shows that although 'Oumuamua looks familiar there are differences that relate to its birth in a solar system far from our own.

Online content

Any Methods, including any statements of data availability and Nature Research reporting summaries, along with any additional references and Source Data files, are available in the online version of the paper at <https://doi.org/10.1038/s41586-018-0254-4>.

Received: 17 April 2018; Accepted: 29 May 2018;

Published online 27 June 2018.

- Meech, K. J. et al. A brief visit from a red and extremely elongated interstellar asteroid. *Nature* **552**, 378–381 (2017).
- Fraser, W. C. et al. The tumbling rotational state of 11/'Oumuamua. *Nature Astron.* **2**, 383–386 (2018).
- Drahus, M. et al. Tumbling motion of 11/'Oumuamua reveals body's violent past. *Nature Astron.* **2**, 407–412 (2018).
- Belton, M. J. S. et al. The excited spin state of 11/2017 U1 'Oumuamua. *Astrophys. J.* **856**, L21 (2018).
- Fitzsimmons, A. et al. Spectroscopy and thermal modelling of the first interstellar object 11/2017 U1 'Oumuamua. *Nature Astron.* **2**, 133–137 (2018).
- Jewitt, D. et al. Interstellar Interloper 11/2017 U1: observations from the NOT and WIYN Telescopes. *Astrophys. J.* **850**, L36 (2017).
- Ye, Q.-Z., Zhang, Q., Kelley, M. S. P. & Brown, P. G. 11/2017 U1 ('Oumuamua) is hot: imaging, spectroscopy, and search of meteor activity. *Astrophys. J.* **851**, L5 (2017).
- Marsden, B. G., Sekanina, Z. & Yeomans, D. K. Comets and nongravitational forces. *V. Astron. J.* **78**, 211–225 (1973).
- Królikowska, M. Long-period comets with non-gravitational effects. *Astron. Astrophys.* **427**, 1117–1126 (2004).
- Wainscoat, R. et al. The Pan-STARRS search for near earth objects. *Proc. IAU* **10**, 293–298 (2015).
- Denneau, L. et al. The Pan-STARRS moving object processing system. *Publ. Astron. Soc. Pacif.* **125**, 357–395 (2013).
- Williams, G.V. MPEC 2017-U181: comet C/2017 U1 (PANSTARRS). *IAU Minor Planet Center* <https://minorplanetcenter.net/mpec/K17/K17U1.html> (2017).
- Engelhardt, T. et al. An observational upper limit on the interstellar number density of asteroids and comets. *Astron. J.* **153**, 133 (2017).
- Farnocchia, D., Chesley, S. R., Milani, A., Gronchi, G. F. & Chodas, P. W. in *Asteroids IV* (eds Michel, P. et al.) 815–834 (Univ. Arizona Press, Tuscan, 2015).
- Prialnik, D. Modeling the comet nucleus interior. *Earth Moon Planets* **89**, 27–52 (2000).
- Park, R. S., Pisano, D. J., Lazio, T. J. W., Chodas, P. W. & Naidu, S. P. Search for OH 18-cm radio emission from 11/2017 U1 with the Green Bank Telescope. *Astron. J.* **155**, 185 (2018).
- Cochran, A. L., Barker, E. S. & Gray, C. L. Thirty years of cometary spectroscopy from McDonald Observatory. *Icarus* **218**, 144–168 (2012).
- Fink, U. A taxonomic survey of comet composition 1985–2004 using CCD spectroscopy. *Icarus* **201**, 311–334 (2009).
- McNeill, A., Trilling, D. E. & Mommert, M. Constraints on the density and internal strength of 11/'Oumuamua. *Astrophys. J.* **857**, L1 (2018).
- Williams, G.V. MPEC 2008-D12: 2006 RH120. *IAU Minor Planet Center* <https://minorplanetcenter.net/mpec/K08/K08D12.html> (2008).
- Micheli, M., Tholen, D. J. & Elliott, G. T. Detection of radiation pressure acting on 2009 BD. *New Astron.* **17**, 446–452 (2012).
- Micheli, M., Tholen, D. J. & Elliott, G. T. 2012 LA, an optimal astrometric target for radiation pressure detection. *Icarus* **226**, 251–255 (2013).
- Micheli, M., Tholen, D. J. & Elliott, G. T. Radiation pressure detection and density estimate for 2011 MD. *Astrophys. J.* **788**, L1 (2014).
- Vokrouhlický, D., Bottke, W. F., Chesley, S. R., Scheeres, D. J. & Statler, T. S. in *Asteroids IV* (eds Michel, P. et al.) 509–531 (Univ. Arizona Press, Tuscan, 2015).
- Meyer-Vernet, N. *Basics of the Solar Wind* 348–351, 366–371 (Cambridge Univ. Press, Cambridge, 2007).
- Zubrin, R. M. & Andrews, D. G. Magnetic Sails and Interplanetary Travel. *J. Spacecr. Rockets* **28**, 197–203 (1991).
- Wang-Sheeley-Arge (WSA)-Enlil Solar Wind Prediction. *Space Weather Prediction Center* <https://www.ngdc.noaa.gov/enlil/> (accessed March 2018).
- Richter, I. et al. Magnetic field measurements during the ROSETTA flyby at asteroid (21) Lutetia. *Planet. Space Sci.* **66**, 155–164 (2012).
- Meech, K. J. et al. Inner solar system material discovered in the Oort cloud. *Sci. Adv.* **2**, e1600038 (2016).
- Yabushita, S. On the effect of non-gravitational processes on the dynamics of nearly parabolic comets. *Mon. Not. R. Astron. Soc.* **283**, 347–352 (1996).

Acknowledgements K.J.M., J.T.K. and J.V.K. acknowledge support through NSF awards AST1413736 and AST1617015, in addition to support for HST programmes GO/DD-15405 and -15447 provided by NASA through a grant from the Space Telescope Science Institute, which is operated by the Association of Universities for Research in Astronomy under NASA contract NAS 5-26555. R.J.W. and R.W. acknowledge support through NASA under grant NNX14AM74G issued to support Pan-STARRS1 through the SSO Near Earth Object Observation Program. D.F., P.W.C. and A.E.P. conducted this research at the Jet Propulsion Laboratory, California Institute of Technology, under a contract with NASA. We thank S. Sheppard for obtaining the Magellan observations, and E. J. Christensen, W. H. Ryan and M. Mommert for providing astrometric uncertainty information related to the Catalina Sky Survey, Magdalena Ridge Observatory and Discovery Channel Telescope observations of 'Oumuamua. This work is based on observations obtained at CFHT, which is operated by the National Research Council of Canada, the Institut National des Sciences de l'Univers of the Centre National de la Recherche Scientifique of France and the University of Hawai'i. It is based in part on observations collected at the European Organisation for Astronomical Research in the Southern Hemisphere under ESO programme 2100.C-5008(A) and in part on observations obtained under programme GS-2017B-DD-7 obtained at the Gemini Observatory, which is operated by AURA under cooperative agreement with the NSF on behalf of the Gemini partnership: NSF (United States), NRC (Canada), CONICYT (Chile), MINCYT (Argentina) and MCT (Brazil). This work is also based on observations made with NASA/ESA HST, obtained at the Space Telescope Science Institute, which is operated by the Association of Universities for Research in Astronomy under NASA contract NAS 5-26555. This work has made use of data from the ESA mission Gaia (<https://www.cosmos.esa.int/gaia>), processed by the Gaia Data Processing and Analysis Consortium (DPAC; <https://www.cosmos.esa.int/web/gaia/dpac/consortium>). Funding for DPAC has been provided by national institutions, in particular the institutions participating in the Gaia Multilateral Agreement.

Reviewer information Nature thanks A. Fitzsimmons, M. Granvik and the other anonymous reviewer(s) for their contribution to the peer review of this work.

Author contributions M.M. discovered the non-gravitational acceleration and extracted the high-precision astrometry from most ground-based observations obtained by the team. D.F. performed the different fits and modelling of the non-gravitational acceleration. K.J.M. secured the HST time and designed the observation programme, computed sublimation dust and gas outgassing limits, and provided the assessment of outgassing. M.W.B. led the design of the HST observations and contributed precision astrometry from HST images. O.R.H. obtained the deep stack of images, searched them for dust and companion, and estimated production rates. D.P. performed the thermal sublimation modelling. N.S. conducted thermal model calculations. H.A.W. managed the HST observations and the initial reduction of images. P.W.C. provided support in analysing possible explanations for the observed non-gravitational acceleration. J.T.K. assembled the deep stack of CFHT data to search for dust and outgassing. R.W. identified and searched pre-discovery images of 'Oumuamua in Pan-STARRS1 data. R.J.W. obtained the observations using CFHT and searched for pre-discovery observations of 'Oumuamua. H.E. contributed to the HST proposal and to the design of the HST observations. J.V.K. and K.C.C. contributed to the HST proposal. D.K. provided support in analysing possible explanations for the observed non-gravitational acceleration. A.E.P. investigated the magnetic hypothesis.

Competing interests The authors declare no competing interests.

Additional information

Extended data is available for this paper at <https://doi.org/10.1038/s41586-018-0254-4>.

Reprints and permissions information is available at <http://www.nature.com/reprints>.

Correspondence and requests for materials should be addressed to M.M.

Publisher's note: Springer Nature remains neutral with regard to jurisdictional claims in published maps and institutional affiliations.

METHODS

Ground-based observations. We found the first evidence of non-gravitational forces acting on ‘Oumuamua in astrometry derived from a set of ground-based optical images obtained with various ground-based telescopes¹. Our first optical follow-up observations were performed with ESA’s 1.0-metre Optical Ground Station (OGS) in Tenerife, Spain, only 13 h after the discovery of ‘Oumuamua. Subsequent deeper observations were conducted with the 3.6-metre CFHT (seven nights), the 8.2-metre ESO VLT Unit Telescope 1 (two nights), and the 6.5-metre Magellan Baade telescope (two nights). The astrometric positions derived from this ground-based dataset, together with the associated error bars, are sufficient to detect the non-gravitational acceleration at a level of significance of about 5σ .

Search for pre-discovery detections. We searched for pre-discovery images of ‘Oumuamua at positions computed from a model trajectory that included the observed non-gravitational acceleration. Pan-STARRS1 observed suitable fields through its broad *w*-band filter on 2017 June 18 and 22 and through its *i*-band filter on 2017 June 17, almost three months before perihelion. During this time, the predicted average brightness of ‘Oumuamua was around $V \approx 26$ (uncertain because of the large amplitude of the light curve of the object), much fainter than the limiting magnitude of Pan-STARRS1. No object was visible in these images at the predicted location.

HST data and astrometry. Images of ‘Oumuamua were obtained with HST in two separate awards of Director’s Discretionary (DD) time. The first set of observations was designed soon after the discovery of ‘Oumuamua, with the primary goal of extending the observational arc to obtain tighter astrometric constraints on the trajectory of the object. Three HST visits were executed on 2017 November 21–22, one visit on 2017 December 12 and a fifth on 2018 January 2. To maximize the length of the orbital arc covered, the last observation was set to be performed as late as possible, assuming that we would know the rotational phase sufficiently well to enable us to catch the steadily fading and only barely detectable target at light-curve maximum. The discovery of non-principal-axis rotation^{2–4} invalidated our assumption of a predictable light curve and motivated a second allocation of four additional HST orbits, added to the final visit, that allowed us to cover ‘Oumuamua in a more sophisticated temporal cadence that was designed to maximize its detectability regardless of light-curve phase. This additional allocation was essential for our final detection.

Each visit used the same basic observing pattern of five 370-second exposures of the full field of WFC3/UVIS, an exposure time that is just long enough to accommodate CCD readout and data-storage overheads without loss of integration time within the allocated single orbit. All images were taken through the extremely broad F350LP filter, chosen for maximum throughput. This strategy was modelled after very similar observations of (486958) 2014 MU₆₉, the target of the New Horizons extended mission, and resulted in a signal-to-noise ratio of approximately 2–3 for a solar-colour object of magnitude $R = 27.5$.

During all observations, HST tracked ‘Oumuamua, and target motions and parallax corrections were applied. As a result, the object appears as a point source in our images and the background-field stars appear as long trails. Because the density of background stars was very low for these observations, the exact placement of our target within the field of view of the instrument had to be adjusted for some visits to ensure that the number of reference stars (3–10) was sufficient for the aimed-at high-precision astrometric solution.

The positions of reference stars were determined from PSF fitting using the Tiny Tim model³¹ and application of a smearing function derived from the HST-centric motion of the object during each exposure. Uncertainties of the resulting position and flux measurements were derived using a Markov chain Monte Carlo sampling algorithm³². The probability density functions (PDFs) from this calculation were then used to update the default world coordinate system (WCS) solution of each image, using the Gaia DR2³³ position of each star as a reference. A PDF was also derived for this final reference WCS.

The position of ‘Oumuamua was computed in the same fashion, except that no smearing function was needed. Object position, flux and a PDF were derived for each frame where possible (a few images were lost to cosmic-ray strikes). In the final visit, our target was detected in only two of the five orbits. Using the WCS PDF for reference, we combined these results to obtain the final sky-plane PDF for the object in each image and then converted the PDF to a Gaussian approximation covariance for use in the fitting of the trajectory of ‘Oumuamua. Whereas the resulting uncertainties are dominated by catalogue errors for the earlier visits, the low signal-to-noise ratio of the object contributes substantially to the error budget for the final visit. The formal uncertainties from this procedure are at most $0.01''$ – $0.02''$.

Accumulated observational dataset. Our attempts to constrain the trajectory of ‘Oumuamua made use of all available astrometric positions. In addition to our own astrometric dataset (see Extended Data Tables 1 and 2), we included all relevant data submitted to the Minor Planet Center, for a total of 177 ground-based observations and 30 HST observations. Seven additional ground-based observations

deemed unreliable by the observers were not considered. Where no uncertainties were provided by the observers, we assumed a $1''$ positional uncertainty, except for a handful of observations that showed poor internal consistency were further de-weighted (these error bars are presented in Extended Data Table 3). Moreover, we assumed that the reported observation times are uncertain by 1 s. Finally, positions that did not use the Gaia DR1 or DR2 catalogue^{33,34} as a reference were corrected for systematic errors of the respective star catalogue³⁵, resulting in corrections as large as $0.4''$ for the USNO-B1.0 catalogue³⁶. To mitigate the effect of unresolved systematic errors, we used an uncertainty floor of $0.05''$ to set the data weights.

Potential biases in the detection of non-gravitational motion. To test whether the detected non-gravitational acceleration could be an artefact introduced by a subset of biased astrometric observations, we used the $A_1 g(r)$, $g(r) \propto r^{-2}$ non-gravitational model. We performed a series of analyses on subsets of the full data arc that were designed to highlight whether specific groups of observations could be responsible for the signal. A summary of our findings is as follows.

The signal is not caused by the early, noisier observations. Fitting only data taken after 2017 October 25 or after 2017 November 15 still yields a detection of A_1 at 17σ and 2.5σ confidence, respectively. Similarly, the signal is not caused by only the late part of the arc. Fitting only data taken before 2017 November 15 or up to 2017 December 1 still yields a detection of A_1 at 2.8σ and 7.4σ confidence, respectively.

To rule out biases in data from ground-based observations, for example, due to colour refraction in the atmosphere, we computed orbital solutions using only HST data and a single ground-based observation set: OGS on October 19, CFHT on October 22 or VLT on October 25. In all three tests, non-gravitational motion was detected at a significance of at least 11σ .

Some of the ground-based astrometric positions for ‘Oumuamua were measured relative to the Gaia DR1 catalogue, which does not include the proper motions of stars. Because Gaia DR1 uses 2015 as the reference epoch, offsets due to proper motions³⁵ could amount to as much as about $0.04''$. The tests that we performed that combine HST and our ground-based astrometry, which was reduced with Gaia DR2, shows that the detection of non-gravitational motion is not caused by this issue.

To rule out the possibility that the detection of non-gravitational motion could be due to issues with HST data (such as in the case of comet C/2013 A1, for which the HST astrometry was found to have larger errors than expected³⁷), we performed a fit using only ground-based observations and still detected non-gravitational motion at 7.1σ significance. To make sure that the high significance of the non-gravitational signal is not caused by overly optimistic assumptions regarding the astrometric uncertainties, we ran a test using an uncertainty floor of $1''$ and still obtained a 7.0σ signal for A_1 .

The results of our tests show that the observed non-gravitational signature is not an artefact of biases in the data or the specifics of the analysis performed, but is indeed present in the motion of ‘Oumuamua.

Non-gravitational models. In addition to $A_1 g(r)$, with $g(r) \propto r^{-2}$, we considered several alternative models for the observed non-gravitational acceleration of ‘Oumuamua. The χ^2 and χ^2_ν values of the corresponding fits to all astrometric data are shown in Table 1 for comparison with the gravity-only reference model. A brief summary of each model (numbered as in Table 1) is provided below.

(1) We searched for evidence of an impulsive change in velocity (Δv) and found two χ^2 minima, one on 2017 November 5 and another on 2017 December 6, both requiring $\Delta v \geq 5 \text{ m s}^{-1}$. However, the corresponding orbital solutions provide a poorer fit to the data than do continuous acceleration models. Moreover, as discussed before, evidence of non-gravitational acceleration is found in the arcs before 2017 December 6 and after 2017 November 5. Therefore, an impulsive Δv event alone cannot model the trajectory of ‘Oumuamua.

(2) We tested different power laws for the radial dependency of the acceleration: $g(r) \propto r^{-k}$, $k \in \{0, 1, 2, 3\}$. A constant $g(r)$ ($k=0$) provides a poorer fit to the data. Within the timespan of our fit, which extends from $r=1.1 \text{ AU}$ to $r=2.9 \text{ AU}$, the acceleration decreases with increasing heliocentric distances at a rate that cannot be much steeper than r^{-2} , but can be gentler, for example, r^{-1} , with both trends having comparable likelihood. On the other hand, a trend of r^{-3} is strongly disfavoured by the data.

(3) Adding transverse ($A_2 g(r)$) and normal (out-of-plane; $A_3 g(r)$) acceleration components to a radial-acceleration-only model (the result is referred to as the RTN model) yields only a modest improvement in the fit, regardless of the dependence on heliocentric distance that we select, showing that the non-gravitational acceleration of ‘Oumuamua is mostly radial. The best-fitting values for A_2 and A_3 are consistent with zero (significance of less than 1σ) and are an order of magnitude smaller than that for A_1 .

(4) Alternatively, the acceleration vector can be decomposed into along-track, cross-track, and normal (ACN) components with respect to the trajectory. The goodness of the resulting fit is comparable to that obtained for the RTN decomposition. However, in the ACN frame all three directions are needed to describe the data, whereas a single parameter is sufficient in the RTN frame.

(5) An unacceptably poor fit is obtained if the acceleration is assumed to act exclusively in the direction of the velocity vector of the object (that is, the along-track component of the ACN frame), for any $g(r) \propto r^{-k}$, $k \in \{0, 1, 2, 3\}$.

(6) We also tested the possibility of a constant acceleration vector, fixed in inertial space. Despite the larger number of estimated parameters, the resulting fit is no better than that obtained with a purely radial acceleration. Moreover, the complex rotation state of 'Oumuamua²⁻⁴ is at odds with such an inertially fixed acceleration.

(7) Finally, we tested non-gravitational models involving cometary activity. A CO-driven³⁰ $g(r)$ (7a and 7c in Table 1) behaves similarly to r^{-2} for $r < 5$ AU and provides a better fit than a H₂O-driven⁸ $g(r)$ (7b and 7d), which falls off like $r^{-2.15}$ for $r < 2.8$ AU and then decays abruptly like r^{-26} . This latter model can include a time offset $\Delta T = 55$ d with respect to perihelion for the acceleration peak³⁸ (7e), thus moving the fast decay of $g(r)$ outside of the data arc.

The difference between χ^2 values for models within a given family (the exponent k for each of models (2), (3), (4) and (5) in Table 1) is useful for statistically evaluating how significantly some exponents are disfavoured with respect to the best-fitting one of the same family.

Limits on cometary activity. We estimate that no more than about 1 kg of 1- μ m-sized dust grains could have been present in the direct vicinity of 'Oumuamua (less than 2.5'' or 750 km from the nucleus) on 2017 October 25–26¹, on the basis of the dust-limiting magnitude for dust $g > 29.8$ mag arcsec⁻². Here we perform the same analysis on deep stacks of the 2017 November 21, 22 and December 1 HST data in search of evidence of dust. To this end, we subtracted a copy of each image from itself after rotation by 180°. Because any dust is pushed from the nucleus by solar-radiation pressure, its distribution is expected to be highly asymmetric. The self-subtraction removes the light from the nucleus and the symmetric component and makes the asymmetric component more prominent. The subtracted frames were further enhanced by wavelet filtering (which boosts the signal with spatial frequencies corresponding to 2–8 pixels) and adaptive smoothing (which smooths the signal over a region with a size adapted dynamically such that the signal-to-noise ratio reaches a threshold, set here to 2). Examination of the resulting images, shown in Fig. 1, does not reveal any sign of dust to a similar limit. The asymmetry test is particularly sensitive for the October 25–26 stack: because the Earth was only 15° above the orbital plane of the object, any dust released from the nucleus since its passage through perihelion is expected to be confined to a narrowly fanning region with position angles of approximately 96°–135°. Our findings thus indicate that the original upper limit of about 1 kg of 1- μ m-sized dust within 750 km on October 25 is conservative (corresponding to $g > 29.8$ mag arcsec⁻² at the 5σ level).

To test this limit, a dust feature was introduced in the images, which were then re-processed using the same enhancement techniques. The feature was produced using a cometary image approximately matching the expected morphology of ejected dust for October 25 (when the geometry was the best to concentrate the dust in a narrow region), scaled to match the photometric contribution in the central 2.5''. This is illustrated in Fig. 1, and indicates that the dust would indeed probably be detected.

From the orbital fits we know that the non-gravitational acceleration on 'Oumuamua on October 25 at $r = 1.4$ AU was $A_1 r^{-2} = 2.7 \times 10^{-6}$ m s⁻¹. The mass m of 'Oumuamua can be estimated from the photometry¹, assuming an albedo of 0.04 (0.2) and a bulk density of less than 500 kg m⁻³ (2000 kg m⁻³) for a cometary³⁹ (asteroidal^{19,40}) object. If the non-gravitational force is due to cometary activity, then Newton's law can be used to relate the observed acceleration to the gas production rate⁴¹ Q : $ma = Q\zeta v_i$, where v_i is the gas ejection velocity and ζ is a poorly constrained, dimensionless efficiency factor that accounts for (among other effects) the geometry of the emission. At the heliocentric distance of 'Oumuamua on October 25 of 1.4 AU, ζv_i would fall between 150 m s⁻¹ and 450 m s⁻¹; in the following, we adopt 300 m s⁻¹. The resulting gas production rates, at a heliocentric distance of 1.4 AU, range from 0.7 kg s⁻¹ to 140 kg s⁻¹ depending of the size, shape and mass of the object, with a mass loss of $Q = 10$ kg s⁻¹ being our best estimate. This value was used to constrain the thermal model discussed in the following.

Thermal model. We carried out thermal model calculations to estimate the interior temperatures that 'Oumuamua reached during its passage. These thermal calculations begin four years before perihelion and end two years after perihelion. The one-dimensional⁴² model resolves the diurnal cycle with at least 288 time steps within each 7.34-hour simple rotation. We assumed an albedo of 0.04 and an obliquity of 45°, and used two parameter combinations: one with a porosity of 40% and a thermal inertia of 400 J m⁻² K⁻¹ s^{-1/2} (at 200 K), and the other with a porosity of 90% and a thermal inertia of 40 J m⁻² K⁻¹ s^{-1/2}. Calculations were carried out for the object's equator (where the surface normal is perpendicular to the rotation axis) and at a latitude of 45°, starting from an initial temperature of 4 K. The depths to maximum temperature along the orbit depend on the assumed physical properties, but for the parameters specified above, which capture a wide range of values, 160 K (the approximate activation threshold for H₂O-driven cometary activity) is reached within the top roughly 1 m of the surface, consistent

with previous results⁵. Because 'Oumuamua is only tens of metres wide, 30 K (the approximate threshold for CO activity) was exceeded within most of the body. The case of CO₂ lies in between (80 K). The model temperatures suggest that if CO ice was present then considerable outgassing occurred, and even CO₂ ice would have experienced substantial sublimation.

Outgassing models. To verify whether cometary activity can produce the observed non-gravitational acceleration, we modelled¹⁵ the object as a comet. Note that, because of the large range of plausible masses for the nucleus, our results should be considered order-of-magnitude estimates. We assumed the following initial physical characteristics for a spherical nucleus¹: a radius of 102 m, an albedo $p = 0.04$, a density $\rho = 500$ kg m⁻³, an ice-to-dust ratio of unity (in mass), 60% porosity and a bulk thermal conductivity of 0.7 W m⁻¹ K⁻¹, all typical values for comets¹⁵. The model considers subsurface H₂O and CO ices (with CO/H₂O = 0.05 by mass) and, following this model nucleus along the trajectory of 'Oumuamua, evaluates the sublimation over a 400-day period centred on perihelion. The water production rate was found to peak close to perihelion and then decline following an r^{-2} profile until 100 days after perihelion (at 2.6 AU in mid-December 2017), when it starts to decrease sharply. At that point, the CO production rate, which does not change much along the trajectory, becomes dominant, and hence the total production rate continues to follow the r^{-2} trend. The gas velocity was estimated at $v_i = 500$ m s⁻¹, within the range of ζv_i values discussed above.

We adjusted additional physical parameters that characterize the model nucleus (such as thermal conductivity, ice-to-dust ratio and bulk density) in an attempt to match $Q_{\text{H}_2\text{O}} = 10$ kg s⁻¹ at 1.4 AU, our estimate of the gas production rate required to generate the observed non-gravitational acceleration. The closest match to the observations resulted from the following model parameters: $\rho = 450$ kg m⁻³, ice/dust = 3 by mass, CO/H₂O = 0.25, 60% porosity for the initial composition and low temperature. The resulting model parameters are mostly within acceptable limits and physically meaningful; for instance, the thermal conductivity required matches that of silicates, rather than that of a mix of silicate and organics. The dust production was estimated using a low drag coefficient, acknowledging that the gas, and therefore the dust, would come from the subsurface. For our initial model, however, $Q_{\text{dust}} = 0.2$ kg s⁻¹ and the maximal gas production at 1.4 AU is $Q_{\text{H}_2\text{O}} = 2.5$ kg s⁻¹, which provides insufficient acceleration. With a much higher CO/H₂O ice ratio, the production rate increases to within a factor of about 2–3 that needed to match the acceleration detected, with a dust production rate of 0.4 kg s⁻¹. A further increase in mass loss by approximately 30% would result if the surface area had an ellipsoidal shape instead of a spherical shape, with the same median photometric cross-section. The dust production rates inferred from the thermal models require the grains to be relatively large (about 100 μ m to a few millimetres) to match the optical non-detection limits for dust. Large grains are typical of outgassing from subsurface layers as seen in laboratory experiments⁴³, and models of the physical interaction of Oort cloud comets and the interstellar medium show that small grains are efficiently removed by drag effects⁴⁴. No model using an asteroid-like density¹⁹ could be made to produce sufficient acceleration. Further, a high bulk density imposes a limit on ice content even for near-zero porosity. Even assuming a very high CO/H₂O ratio, the maximum outgassing is more than an order of magnitude too low. Finally, acceleration from outgassing reaches the required value if the assumed density of 'Oumuamua is lowered to around 200 kg m⁻³. Although other values could be obtained by adjusting the dust size distribution and the nucleus pore size, further exercises would be of little benefit, as long as we do not have additional constraints.

In conclusion, we find that sublimation can account for the non-gravitational forces that were measured, when modelling 'Oumuamua as a small comet, but only if it has some unusual properties.

Consequences of the analysis for the study of the origin of 'Oumuamua. The many uncertainties and assumptions in the non-gravitational models presented here limit our ability to fully determine the past history of 'Oumuamua. These limitations are intrinsically due to the absence of observational information on the behaviour of the non-gravitational acceleration outside the observed arc. In particular, the absence of information on the behaviour of the non-gravitational acceleration before the time of discovery implies that it is much more difficult (and subject to much larger uncertainties) to extrapolate the motion of 'Oumuamua to its original incoming direction.

Solar-radiation pressure. A simple radial dependency of the non-gravitational acceleration, decaying as r^{-2} with the heliocentric distance, is allowed by the dataset for $A_1 = (4.92 \pm 0.16) \times 10^{-6}$ m s⁻². If interpreted as solar-radiation pressure on the projected area of the object exposed to sunlight, then this A_1 value would correspond to an area-to-mass ratio between about 0.5 m² kg⁻¹ and 1 m² kg⁻¹. Given the range of possible sizes and shapes of 'Oumuamua¹, and assuming a uniform density and an ellipsoidal shape for the body, this estimate of the area-to-mass ratio would correspond to a bulk density of the object between about 0.1 kg m⁻³ and 1 kg m⁻³, three to four orders of magnitude less than that of water. Alternatively, to be composed of materials with densities comparable to normal asteroidal or cometary

matter, 'Oumuamua would need to be a layer, or a shell, at most a few millimetres thick, which is not physically plausible.

Unless 'Oumuamua has physical properties that differ markedly from those of typical Solar System bodies within the same size range, the interpretation of the non-gravitational acceleration being due to solar-radiation pressure is therefore unlikely.

Binary object or fragmentation event. The existence of one or more fragments could theoretically explain the detected astrometric offsets by displacing the centre of mass of the overall system from the main component that was measured astrometrically. However, the existence of a bound secondary body of substantial mass can easily be discounted both directly and indirectly.

The offsets from a gravity-only solution (see Fig. 2) observed at the time of our deepest images are at the arcsecond level, requiring a possible bound secondary body to have a separation from the main mass that is comparable or greater than this distance. However, no co-moving object was detected in the vicinity of the main body, although most of the images we obtained with large-aperture telescopes have subarcsecond resolution and reach a depth a few magnitudes fainter than 'Oumuamua. Specifically, the limiting magnitudes estimated from the signal-to-noise ratio of 'Oumuamua on deep stacks of data from VLT (October 25), GS (October 26) and HST (November 21 and 22) are $r'_{\text{lim}} = 27.0$ and $V_{\text{lim}} = 29.2$, respectively. Conversion to an upper limit for the radius of an unseen object yields 7.8 m (3.5 m) and 4.5 m (2.0 m), respectively, for an albedo of 0.04 (0.2), typical for a cometary (an asteroid) nucleus—about 100 times smaller than the main body using the same assumptions. In addition, given the small mass of 'Oumuamua, the radius of its sphere of influence $r \propto a(m/M)^{2/5}$ (where a is the distance between the object and the Sun and m and M the masses of the object and the Sun, respectively) is of the order of 1 km, corresponding to angular separations of milliarcseconds. Any object within such a distance would be fully embedded in the PSF of the main body and therefore would not contribute any detectable offset to the astrometric photocentre.

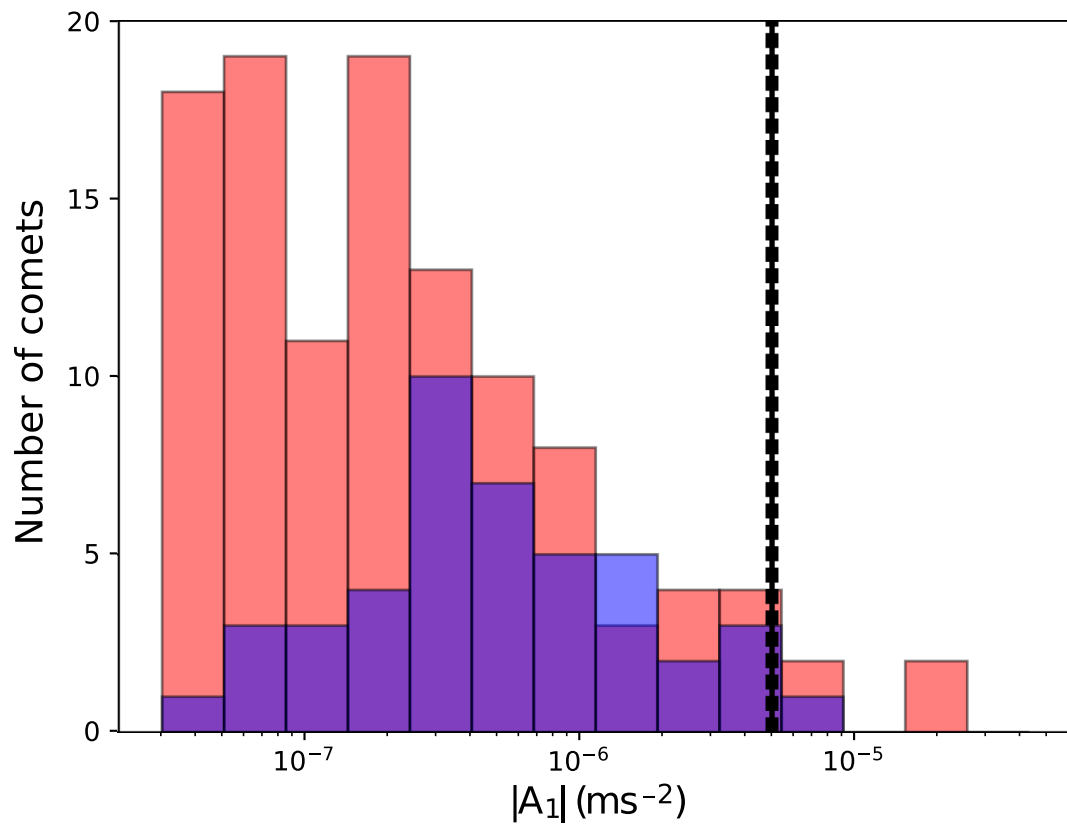
The possibility of an unbound fragment being ejected by 'Oumuamua during the observed arc can also be excluded, not only because no such fragment was seen in the deep images we obtained, but also because its dynamical effect would correspond to an impulse-like event in the trajectory, which we have already shown to be incompatible with the data.

Code availability. The JPL asteroid and comet orbit determination code, used in the in-depth analysis of the possible dynamical scenarios, is proprietary. However, some key results of this analysis, including the detection of a significant non-gravitational acceleration at the 30σ level, can easily be reproduced by using freely

available software such as Find_Orb (https://www.projectpluto.com/find_orb.htm). The code for the comet sublimation model is a direct implementation of a published model^{15,45}. Source code and further documentation for the type of one-dimensional thermal model used is available at <https://github.com/nschorgh/Planetary-Code-Collection/>.

Data availability. The astrometric positions and uncertainties on which this analysis is based are available in Extended Data Tables 1–3, and will be submitted to the Minor Planet Center for public distribution. Source Data for Fig. 2 and Extended Data Fig. 1 is available with the online version of the paper.

31. Krist, J. E., Hook, R. N. & Stoehr, F. 20 years of Hubble Space Telescope optical modeling using Tiny Tim. *Proc. SPIE* **8127**, 81270J (2011).
32. Hastings, W. K. Monte Carlo sampling methods using Markov chains and their applications. *Biometrika* **57**, 97–109 (1970).
33. Gaia Collaboration. Gaia data release 2. Summary of the contents and survey properties. *Astron. Astrophys.* <https://doi.org/10.1051/0004-6361/201833051> (2018).
34. Lindegren, L. et al. Gaia data release 1. Astrometry: one billion positions, two million proper motions and parallaxes. *Astron. Astrophys.* **595**, A4 (2016).
35. Farnocchia, D., Chesley, S. R., Chamberlin, A. B. & Tholen, D. J. Star catalog position and proper motion corrections in asteroid astrometry. *Icarus* **245**, 94–111 (2015).
36. Monet, D. G. et al. The USNO-B catalog. *Astron. J.* **125**, 984–993 (2003).
37. Farnocchia, D. et al. High precision comet trajectory estimates: the Mars flyby of C/2013 A1 (Siding Spring). *Icarus* **266**, 279–287 (2016).
38. Yeomans, D. K. & Chodas, P. W. An asymmetric outgassing model for cometary nongravitational accelerations. *Astron. J.* **98**, 1083–1093 (1989).
39. A'Hearn, M. F. Comets as building blocks. *Annu. Rev. Astron. Astrophys.* **49**, 281–299 (2011).
40. Carry, B. Density of asteroids. *Planet. Space Sci.* **73**, 98–118 (2012).
41. Crovisier, J. & Schloerb, F. P. in *Comets in the Post-Halley Era* (eds Newburn, R. L. et al.) 166 (Kluwer, The Netherlands, 1991).
42. Schorghofer, N. The lifetime of ice on main belt asteroids. *Astrophys. J.* **682**, 697–705 (2008).
43. Laufer, D., Pat-El, I. & Bar-Nun, A. Experimental simulation of the formation of non-circular active depressions on comet Wild-2 and of ice grain ejection from cometary surfaces. *Icarus* **178**, 248–252 (2005).
44. Stern, S. A. ISM-induced erosion and gas-dynamical drag in the Oort cloud. *Icarus* **84**, 447–466 (1990).
45. Prialnik, D. Crystallization, sublimation, and gas release in the interior of a porous comet nucleus. *Astrophys. J.* **388**, 196–202 (1992).
46. Vereš, P., Farnocchia, D., Chesley, S. R. & Chamberlin, A. B. Statistical analysis of astrometric errors for the most productive asteroid surveys. *Icarus* **296**, 139–149 (2017).



Extended Data Fig. 1 | Non-gravitational accelerations of Solar System comets and 'Oumuamua. Measured non-gravitational radial accelerations A_1 for short-period (red) and long-period (blue) comets from the JPL Small Body Database (<https://ssd.jpl.nasa.gov/sbdb.cgi>). The solid vertical

black line indicates the A_1 value for 'Oumuamua, which falls within the range observed for Solar System comets; the dashed vertical black lines mark the corresponding 1σ uncertainty.

Extended Data Table 1 | Ground-based astrometry

Date (UTC)	R.A.	Dec.	$\sigma_{\text{R.A.}}$ (")	$\sigma_{\text{Dec.}}$ (")	Obs. code
2017-10-18.472979	01 59 57.460	+02 06 04.02	1.00	1.00	F51
2017-10-18.499898	01 59 08.928	+02 07 20.53	1.50	1.50	F51
2017-10-19.397150	01 34 55.364	+02 45 03.09	0.40	0.40	F51
2017-10-19.408370	01 34 38.761	+02 45 28.19	0.40	0.40	F51
2017-10-19.419685	01 34 21.996	+02 45 53.47	0.40	0.40	F51
2017-10-19.431056	01 34 05.210	+02 46 18.48	1.00	1.00	F51
2017-10-19.940934	01 22 22.290	+03 03 53.82	0.20	0.20	J04
2017-10-19.943901	01 22 18.370	+03 03 59.58	0.20	0.20	J04
2017-10-22.371415	00 40 57.815	+04 02 50.75	0.05	0.05	568
2017-10-22.372590	00 40 56.875	+04 02 52.02	0.05	0.05	568
2017-10-22.373983	00 40 55.762	+04 02 53.49	0.05	0.05	568
2017-10-23.384311	00 28 51.402	+04 19 02.21	0.15	0.15	568
2017-10-23.385548	00 28 50.593	+04 19 03.41	0.15	0.15	568
2017-10-23.386852	00 28 49.730	+04 19 04.54	0.15	0.15	568
2017-10-25.044458	00 13 18.796	+04 39 35.19	0.05	0.05	309
2017-10-25.050182	00 13 15.981	+04 39 38.79	0.05	0.05	309
2017-10-25.061553	00 13 10.389	+04 39 45.94	0.05	0.05	309
2017-10-25.112088	00 12 45.650	+04 40 17.26	0.05	0.05	309
2017-10-25.117597	00 12 42.966	+04 40 20.70	0.05	0.05	309
2017-10-26.133749	00 05 15.166	+04 49 55.54	0.06	0.06	309
2017-10-26.138575	00 05 13.175	+04 49 58.07	0.06	0.06	309
2017-10-26.143286	00 05 11.230	+04 50 00.52	0.06	0.06	309
2017-10-26.185052	00 04 54.100	+04 50 21.91	0.06	0.06	309
2017-10-27.269327	23 58 14.606	+04 58 44.31	0.06	0.06	568
2017-10-27.282873	23 58 09.917	+04 58 50.36	0.06	0.06	568
2017-10-27.304553	23 58 02.427	+04 58 59.94	0.05	0.05	568
2017-10-27.330214	23 57 53.596	+04 59 11.15	0.10	0.10	568
2017-10-27.381822	23 57 35.926	+04 59 33.51	0.10	0.10	568
2017-11-15.306018	23 18 51.738	+06 14 13.51	0.06	0.06	568
2017-11-15.309275	23 18 51.633	+06 14 14.10	0.06	0.06	568
2017-11-15.312534	23 18 51.529	+06 14 14.66	0.06	0.06	568
2017-11-15.315806	23 18 51.418	+06 14 15.25	0.06	0.06	568
2017-11-16.207482	23 18 27.240	+06 16 59.12	0.10	0.10	568
2017-11-16.210740	23 18 27.141	+06 16 59.74	0.10	0.10	568
2017-11-16.213997	23 18 27.045	+06 17 00.34	0.10	0.10	568
2017-11-16.217253	23 18 26.956	+06 17 00.94	0.10	0.10	568
2017-11-21.026940	23 17 05.962	+06 32 01.74	0.10	0.10	304
2017-11-21.032458	23 17 05.893	+06 32 02.84	0.10	0.10	304
2017-11-21.038153	23 17 05.834	+06 32 04.03	0.10	0.10	304
2017-11-21.043922	23 17 05.765	+06 32 05.08	0.10	0.10	304
2017-11-21.060925	23 17 05.573	+06 32 08.23	0.10	0.10	304
2017-11-21.066145	23 17 05.522	+06 32 09.11	0.10	0.10	304
2017-11-21.081650	23 17 05.348	+06 32 12.17	0.10	0.10	304
2017-11-22.222847	23 16 57.168	+06 35 44.32	0.05	0.05	568
2017-11-22.246144	23 16 56.979	+06 35 48.63	0.05	0.05	568
2017-11-22.269437	23 16 56.790	+06 35 53.21	0.05	0.05	568
2017-11-22.292688	23 16 56.602	+06 35 57.52	0.05	0.05	568
2017-11-22.316355	23 16 56.416	+06 36 02.00	0.05	0.05	568
2017-11-23.038940	23 16 53.146	+06 38 25.80	0.12	0.12	304
2017-11-23.070610	23 16 52.967	+06 38 32.02	0.12	0.12	304
2017-11-23.274337	23 16 52.324	+06 39 06.39	0.05	0.05	568
2017-11-23.288299	23 16 52.248	+06 39 09.09	0.10	0.10	568
2017-11-23.373957	23 16 51.831	+06 39 25.49	0.12	0.12	568

Ground-based astrometric positions obtained by our team, with associated 1σ errors, as used in our analysis. For observations with codes F51 or J04, we list the manual re-measurements and associated astrometric errors that we used here, rather than the values available from the Minor Planet Center.

Extended Data Table 2 | HST astrometry

Date (UTC)	R.A.	Dec.	X (km)	Y (km)	Z (km)
2017-11-21.13949584	23:17:05.4011	+06:32:22.611	+1797.7	-6042.7	-2854.2
2017-11-21.14575732	23:17:05.1408	+06:32:24.547	+4946.6	-3541.9	-3298.4
2017-11-21.15201917	23:17:04.8217	+06:32:25.137	+6404.8	+0169.5	-2612.2
2017-11-21.15828066	23:17:04.5335	+06:32:24.580	+5671.7	+3822.4	-1030.1
2017-11-21.16454214	23:17:04.3574	+06:32:23.480	+2994.9	+6164.9	+0905.8
2017-11-21.20571103	23:17:04.8264	+06:32:35.174	+1795.0	-6038.1	-2865.8
2017-11-21.21197288	23:17:04.5677	+06:32:37.090	+4948.6	-3540.6	-3296.8
2017-11-21.21823436	23:17:04.2498	+06:32:37.665	+6410.7	+0166.7	-2598.0
2017-11-21.22449584	23:17:03.9643	+06:32:37.108	+5679.5	+3816.6	-1008.1
2017-11-21.23075732	23:17:03.7895	+06:32:36.014	+3002.0	+6158.1	+0928.0
2017-11-22.53035214	23:16:55.8284	+06:36:47.893	+1959.5	-5866.8	-3104.3
2017-11-22.53661399	23:16:55.5985	+06:36:49.486	+5131.8	-3358.1	-3206.3
2017-11-22.54287547	23:16:55.3158	+06:36:49.816	+6549.9	+0298.0	-2209.5
2017-11-22.54913695	23:16:55.0673	+06:36:49.160	+5726.3	+3851.8	-0454.7
2017-11-22.55539843	23:16:54.9275	+06:36:48.169	+2939.8	+6084.8	+1456.3
2017-12-12.06468176	23:20:53.3768	+07:45:46.658	+1679.8	-6660.5	+0794.3
2017-12-12.07094324	23:20:53.4111	+07:45:47.298	+4666.2	-4478.2	+2443.6
2017-12-12.07720509	23:20:53.3935	+07:45:48.323	+6052.6	-0759.9	+3252.8
2017-12-12.08346657	23:20:53.3819	+07:45:49.844	+5364.0	+3218.8	+2943.9
2017-12-12.08972805	23:20:53.4283	+07:45:51.864	+2836.8	+6094.0	+1623.1
2018-01-02.32061993	23:31:48.3214	+09:16:31.366	+1638.4	-6507.3	+1657.0
2018-01-02.32688178	23:31:48.4836	+09:16:34.181	+4853.0	-4919.9	-0229.1
2018-01-02.33314327	23:31:48.5971	+09:16:36.832	+6402.6	-1644.4	-2036.4
2018-01-02.33940475	23:31:48.7038	+09:16:38.996	+5759.0	+2194.7	-3144.5
2018-01-02.34566623	23:31:48.8412	+09:16:40.537	+3145.7	+5283.4	-3174.2
2018-01-02.45306216	23:31:53.0509	+09:17:08.097	+1635.1	-6519.2	+1612.9
2018-01-02.45932364	23:31:53.2126	+09:17:10.921	+4843.1	-4927.1	-0279.6
2018-01-02.46558512	23:31:53.3287	+09:17:13.563	+6389.8	-1644.4	-2076.1
2018-01-02.47184697	23:31:53.4347	+09:17:15.725	+5747.8	+2202.1	-3159.8
2018-01-02.47810845	23:31:53.5703	+09:17:17.228	+3139.8	+5295.5	-3159.8

Full set of HST-based astrometric positions used here, together with the corresponding geocentric location of the spacecraft in equatorial J2000.0 Cartesian coordinates. Uncertainties of 0.05" were assumed for these observations in our orbital analysis.

Extended Data Table 3 | Uncertainty assumptions for existing astrometry

Obs. code	Date (UTC)	$\sigma_{\text{R.A.}}$ (")	$\sigma_{\text{Dec.}}$ (")
703	2017 October 14, 17	2	2
246	2017 October 19	3	3
Q62	2017 October 22	3	3
G96	2017 October 25	*	*
850	2017 October 27	6	6
H01	2017 October 28, 29, 30	0.3	0.3
705	2017 October 29	3	3
G37	2017 October 30	*	*
H01	2017 November 9, 10, 12	0.3	0.3
G37	2017 November 11	0.3	0.3
H01	2017 November 17	0.5	0.5

Adopted uncertainties for astrometry obtained by other observers and publicly available through the Minor Planet Center. For all observations not listed in this table, we conservatively⁴⁶ adopted uncertainties of 1". Observations marked with an asterisk in the error columns were deemed unreliable by the respective observers and hence excluded from our analysis. Finally, the uncertainties listed for 703, H01 and G37 were obtained through direct communication with the corresponding observers.